Applied Physics A (2024) 130:369
https://doi.org/10.1007/s00339-024-07519-2

Applied Physics A
Materials Science & Processing

Structural and optical properties of semiconductor ZnO nanoparticles synthesized using *Rubus glaucus* extract for enhanced photocatalytic activity

E. Silva[1] · V. M. Orozco-Carmona[2] · A. Castro-Beltran[1] · P. A. Luque[3]

Received: 9 February 2023 / Accepted: 15 April 2024 / Published online: 4 May 2024

Abstract
This study details the synthesis, characterization, and photocatalytic efficacy of zinc oxide (ZnO) nanoparticles (NPs) obtained through an environmentally friendly method with varying quantities of *Rubus glaucus* as a chelating agent. Examination of X-ray Diffraction (XRD) and Transmission Electron Microscopy (TEM) data unveiled ZnO NPs featuring a wurtzite structure and sizes ranging from 43.39 to 28.01 nm. The analysis indicated that the presence of *Rubus glaucus* extract during synthesis influenced the size and band gap of the ZnO NPs, resulting in a decrease from 2.8 to 2.5 eV. The photocatalytic performance of ZnO NPs was assessed through the degradation of synthetic dyes methylene blue (MB), methyl orange (MO), and rhodamine B (RhB). The results demonstrated enhanced photocatalytic activity for the ZnO NPs, with ZnO-RG3 exhibiting the most effective degradation. Under UV light, ZnO-RG3 degraded 99%, 95%, and 95% of MB, MO, and RhB within 90 min, while under sunlight, it achieved degradation rates of 98%, 85%, and 95% for MB, MO, and RhB within the same timeframe. These findings underscore the effectiveness of *Rubus glaucus* extract as a chelating agent in producing metal oxide nanoparticles with remarkable photocatalytic performance under both UV and sunlight conditions.

Keywords ZnO · Rubus glaucus · Semiconductor · Photocatalysis

1 Introduction

One of the biggest challenges nowadays is the supply of quality water to the population. Although water is an indispensable resource for human life, it has been estimated that over a billion people lack access to clean water [1]. While there are various factors limiting access to water, such as climate change and the exponential growth of the population in recent years, water pollution stands out as particularly challenging [2]. A significant portion of this pollution comes mainly from the waste generated by various industries. Among them, the textile industry is responsible for the discharge of large amounts of wastewater containing heavy metals and synthetic dyes [3]. These dyes are generally synthetic compounds with aromatic structures resistant to biological treatments and cause various problems in water effluents, such as eutrophication of the aquatic ecosystem. In addition, these compounds cause health problems in humans, ranging from skin irritation, gastrointestinal problems, and headaches to blindness or even cancer [4]. Therefore, safely removing these dyes from water has become increasingly important. However, the commonly used procedures have some disadvantages: the physical methods are not destructive and can only transfer the dye from one medium to another, while chemical methods generate secondary waste in the form of sludge [5].

A promising alternative to the conventional methods are the so-called advanced oxidation processes (AOP); these methods focus on the degradation of various organic compounds through oxidation reactions [6]. Out of these,

✉ A. Castro-Beltran
andres.castro@uas.edu.mx

✉ P. A. Luque
pluque@uabc.edu.mx

[1] Fuente de Poseidon y Prol. Angel Flores S/N, Universidad Autonoma de Sinaloa, C.P. 81223 Los Mochis, Sinaloa, Mexico

[2] Centro de Investigacion en Materiales Avanzados, S.C., Ave. Miguel de Cervantes 120, Complejo Industrial Chihuahua, C.P. 31109 Chihuahua, Chihuahua, Mexico

[3] Universidad Autonoma de Baja California, Carretera Transpeninsular Ensenada-Tijuana 3917, Colonia Playitas, C.P. 22860 Ensenada, Baja California, Mexico

photocatalysis is a method in which a photocatalyst material is exposed to a light source to break down organic molecules into CO_2, H_2O, and non-toxic mineralized compounds, resulting in the complete degradation of the dyes [7]. This photocatalytic process starts when the photocatalyst is irradiated with a source of light with energy equal to or higher than the band gap of the photocatalyst, causing the electrons of the valence band (BV) to enter an excited state and move to the conduction band (BC), producing electron–hole pairs (e^--h^+). When water molecules interact with the e^--h^+ pairs, they form reactive species that then interact with organic dye molecules and break them down into smaller, less toxic by-products [8].

The most used photocatalyst materials are semiconductors, mainly metal oxides including TiO_2, FeO, SnO_2, and ZnO, widely studied and used in photocatalytic applications [9]. Among them, ZnO is a semiconductor with excellent chemical stability and high catalytic activity. It is also non-toxic, inexpensive, and readily available [10]. As a result, ZnO has seen application in various areas, including electronics, medicine, energy, agriculture, and even consumer products such as sunscreen or makeup. Thanks to its properties, it has also been applied in the degradation of organic pollutants for water treatment [11]. There have been several works reporting on the synthesis of semiconductor NPs for use in photocatalysis [12, 13]. However, ZnO has some limitations: the band gap of ZnO (3.7 eV) only permits activation by UV light, which represents a small fraction of sunlight (3–5%); and second, the fast recombination of the electron–hole pair leads to a delay in the oxidation reactions, thus decreasing the efficiency [14]. To resolve these limitations, various alternatives have been studied, namely doping [15], the formation of nanocomposites with other materials [16], or photosensitization using dyes [17].

On the other hand, while a variety of procedures have been used to synthesize ZnO, the most common chemical methods tend to be expensive, in addition to requiring the use of potentially dangerous and toxic reagents that can cause problems for the environment [18]. Due to this, the development of green synthesis methods has gained interest, as they are safer, cheaper, and more environmentally friendly [19]. These green synthesized NPs have been applied in several fields, such as medicine [20], agriculture [21], construction [22], and water treatment [12]. For the most part, green synthesis refers to a process in which chemical reagents are replaced by biocomponents such as fungi, algae, bacteria, or plants. Among these, the most widely used are plants, as the leaves, fruits, roots, stems or seeds can be used to obtain extracts with large amounts of phytochemical compounds (phenols, flavonoids, saponins, polysaccharides) that can act as chelating agents to form complexes with metal ions during NP synthesis [23]. The blackberry plant (scientific name *Rubus glaucus*) is a plant of the *Rosacea* family native to South America (Ecuador, Costa Rica, Colombia, and Mexico) [24]. This plant's fruits are dark red and have been considered a good source of antioxidants, as they are rich in a variety of the organic compounds favorable to green synthesis [25], such as tannins, quercetin, and anthocyanins [26]. In this study, we aim to report for the first time the effect of different Rubus glaucus concentrations on the structural and optical properties of ZnO NPs, as well as their photocatalytic performance under both UV and sunlight irradiation through the degradation of three different dyes.

2 Experimental

2.1 Materials

The reagents used for the synthesis of nanoparticles were zinc nitrate ($Zn(NO_3)_2$, Sigma-Aldrich) and *Rubus glaucus* fruit (purchased from local stores). For the photocatalytic studies three different dyes were used: methylene blue (MB, 85% purity, FagaLab), methyl orange (MO, 99% purity, FagaLab) and rhodamine B (RhB, 85% purity, FagaLab).

2.2 Preparation of *Rubus glaucus* extract

The *Rubus glaucus* extract was prepared using a simple infusion procedure. First, the *Rubus glaucus* fruits were washed and cut into small pieces. Afterwards, 100 g of the cut fruit was added to a beaker with 100 ml deionized water. This mixture was then heated to 90 °C for 1 h, after which the extract was filtered using a No. 4 Whatman paper filter to remove any solids.

2.3 Synthesis of ZnO NPs

To obtain the ZnO NPs, different amounts of the prepared extract (3, 5 and 8 ml) and diluted in water until reaching a total volume of 40 ml. Then 2 g of zinc nitrate were added to the extract solutions and the samples were stirred magnetically for 1 h. Following this, they were left uncovered at 60 °C for 14 h to evaporate until they reached a syrup-like viscosity. The resulting material was then placed in an oven at 400 °C for 1 h, and then ground into powder once cooled down. The obtained ZnO NPs were labeled as ZnO-RG1, ZnO-RG2, and ZnO-RG3.

2.4 Characterization

Fourier-transform infrared (FTIR) spectra were acquired on a Spectrum Two Perkin Elmer spectroscope. Ultraviolet–visible (UV–vis) spectra were acquired in absorbance mode on a Lamda 365 Perkin Elmer UV–vis spectrophotometer. The thermal stability of the NPs was investigated

using SDT Q600 TA INSTRUMENTS thermogravimetric analyzer. X-ray diffraction (XRD) patterns were obtained through a Panalytical X-Pertsystem diffractometer using a Cu Kα radiation source. The Raman spectra were obtained with a microRaman HR spectrometer. The morphology of the NPs was observed using transmission electron microscopy (TEM) obtained through a JEOL JEM-2200FS + Cs microscope. The binding energy and elemental compositions were analyzed X-ray photoelectron spectroscopy (XPS) using a SPECS PHOIBOS 100 analyzer and a SPECS Focus 500 monochromatic Al Kα source.

2.5 Photocatalytic activity assay

The performance of the obtained ZnO NPs was evaluated through the photodegradation of three different dyes (MB, MO, and RhB, all at a concentration of 15 mg/L). For both the UV and solar radiation experiments, typically, the ZnO NPs (ZnO-RG1, ZnO-RG2, and ZnO-RG3) were added to the dye solutions in a 1:1 w/v ratio and stirred in total darkness for 30 min. Afterward, for UV light photocatalysis, the dye/photocatalyst mixtures were irradiated with UV light from a 10 W lamp for 3 h. For the solar photocatalysis evaluation, the solutions were placed under solar irradiation for 3 h (11:00–14:00 on July, in Ensenada, B. C., Mexico). In both cases, aliquots were taken every 10 min until 30 min, and then every 30 min. Then, the absorbance was measured through UV–vis spectroscopy to analyze the concentration.

3 Results and discussion

3.1 Fourier-transform infrared spectroscopy (FTIR)

The FTIR spectra of ZnO-RG1, ZnO-RG2, and ZnO-RG3 are shown in Fig. 1. For ZnO-RG1, the presence of a band at 3276 cm^{-1} is observed, this band corresponds to the stretching of the OH bond. Another band at 1647 cm^{-1} is attributed to C=C bond vibrations characteristic of aromatic rings. The bands at 1442 cm^{-1} and 1362 cm^{-1} are assigned to OH-bending bonds of the polyphenols, confirming the presence of aromatic groups. Finally, bands corresponding C–O–C and OH bonds of phenolic groups are observed at 1122 cm^{-1} and 1024 cm^{-1}. These results are in agreement with what has been previously reported for *Rubus glaucus* extract [27]. In addition, a small band can be observed around 618 cm^{-1}, which is assigned to Zn–O bond vibrations [28]. The presence of these bands indicates that the extract has been functionalized with the ZnO NPs, most likely by complexing the Zn^{2+} metal ions with the hydroxyl or carboxyl groups of the organic molecules from the extract [29]. These same signals can be observed for the ZnO-RG2 and ZnO-RG3 samples, with a slight increment in the relative intensity of the signals

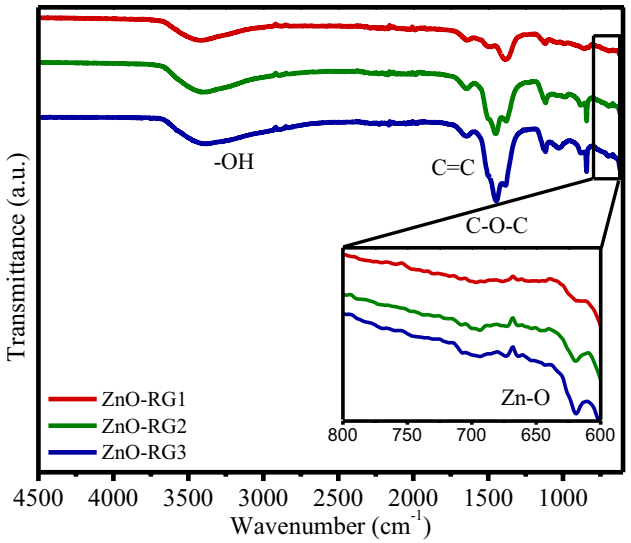

Fig. 1 FTIR spectra for the green synthesized ZnO NPs

associated with the functional groups of the extract as the concentration increases. This suggests that more organic components were functionalized to the ZnO surface.

3.2 UV–vis spectroscopy

The UV–vis spectra for ZnO-RG1, ZnO-RG2, and ZnO-RG3 are shown in Fig. 2a. In the spectra for ZnO-RG1, we can observe a peak around 350–400 nm, which is associated with ZnO surface plasmon resonance and fits the values previously reported by other works [30]; this same peak is observed for all three samples, confirming the synthesis of ZnO. Additionally, the narrow bands are indicative of nanometric particles [31].

The UV–vis absorption data was also analyzed to obtain the band gap value for the samples according to the TAUC model [32]. These results are presented in Fig. 2b, where we can observe band gap values of 2.88 eV, 2.73 eV, and 2.54 eV for ZnO-RG1, ZnO-RG2, and ZnO-RG3, respectively. Furthermore, it is shown that there was a decrease in the bandgap value when a higher amount of extract was used for synthesis. This difference in the bandgap values can be related to quantum confinement caused by size reduction observed on TEM results [33], as well as the presence of oxygen vacancies left behind during calcination of the organic material from the extract, which has been reported to cause band gap narrowing [34].

3.3 Thermogravimetric analysis (TGA)

Figure 3 shows the TGA curve for the ZnO-RG1, ZnO-RG2, and ZnO-RG3 samples. Analyzing the curve, we can observe a weight loss at around 100 °C associated with the

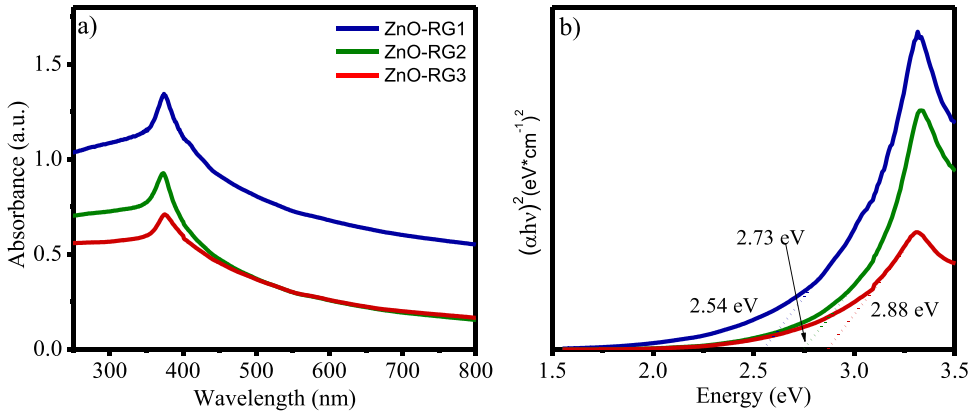

Fig. 2 **a** UV–vis spectra and **b** bandgap values of the obtained ZnO NPs

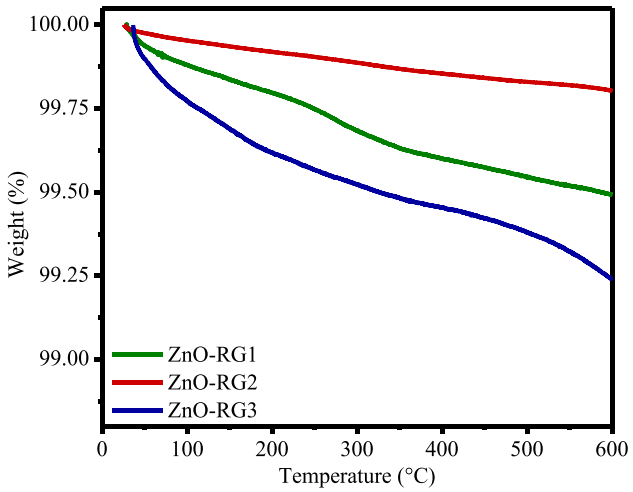

Fig. 3 Thermogravimetric analysis of the obtained ZnO NPs

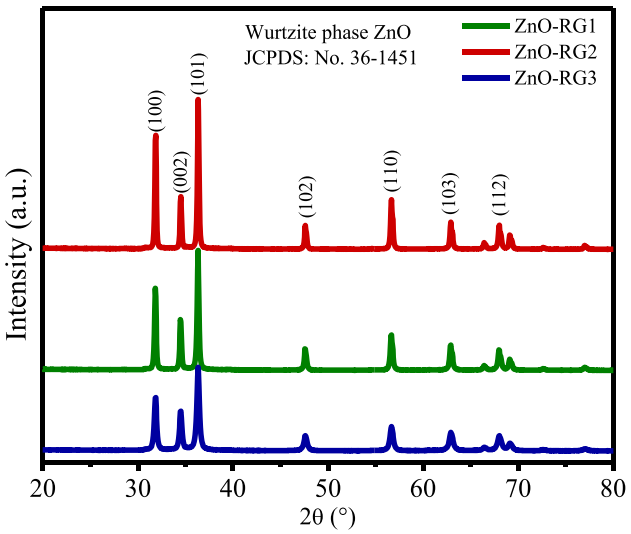

Fig. 4 XRD patterns of the obtained ZnO NPs

evaporation of surface-adsorbed water. The weight loss in the 340–500 °C range can be attributed to the decomposition of the organic molecules from *Rubus glaucus* still present in the material, releasing CO_2 and water [35]. Furthermore, it is important to note that the total weight loss for all three samples is less than 1%, indicating that the obtained NPs have high purity and excellent thermal stability [36].

3.4 X-ray diffraction (XRD)

X-ray diffraction patterns were obtained to analyze and identify the structure of the obtained ZnO NPs. The XRD data for ZnO-RG1, ZnO-RG2, and ZnO-RG3 is displayed in Fig. 4. In the case of ZnO-RG1, we can observe well-defined peaks located at 31.86°, 34.51°, 36.34°, 47.63°, 56.69°, 62.95° and 68.1°, which correspond to (100), (002), (101), (102), (110), (103) and (112) planes. These results have been matched to JCPDS card no. 36-1451, identifying the structure as ZnO in a wurtzite-type hexagonal phase [37]. The sharp and narrow shape of these peaks confirms the ZnO NPs have a highly crystalline structure. Additionally, the absence of extraneous signals indicates a single-phase structure without impurities. Similarly, for samples ZnO-RG2 and ZnO-RG3, the same well-defined peaks are observed, which confirms that all 3 ZnO samples present a crystalline character.

The XRD data was also analyzed using Scherrer's formula to obtain the crystallite size of the nanoparticles [38]. The average crystallite size was 41.82 nm, 37.63 nm, and 26.00 nm for ZnO-RG1, ZnO-RG2, and ZnO-RG3, respectively. Furthermore, there is a notable decrease in crystallite size for the NPs synthesized with higher amounts of extract. This decrease in size is a behavior that has been previously reported and is explained by the biomolecules from the extract acting as stabilizing/capping agents, limiting crystal growth during the formation of the NPs. With a higher amount of extract, more biomolecules are involved during synthesis and, thus, less growth [46].

3.5 Raman spectroscopy

The Raman spectra for the ZnO NPs (ZnO-RG1, ZnO-RG2, and ZnO-RG3) are shown in Fig. 5. For ZnO-RG1, we can observe a peak at 332 cm^{-1}, which is characteristic to E_{2H}–E_{2L} (E_{2LOW}) multi-phonon process. The second peak at 386 cm^{-1} is attributed to the $A_{1(TO)}$ phonon mode, which indicates the presence of oxygen vacancies or interstitial zinc [39]; these vacancies are attributed to lattice defects left behind by the calcination of organic molecules from the extract used for the synthesis. Finally, the peak located at 443 cm^{-1} is associated with the $E_{2(high)}$ vibrational mode that is characteristic of the wurtzite phase of ZnO [40], confirming that we have successfully obtained ZnO. Its higher intensity and sharpness compared to the rest of the peaks indicates the NPs are crystalline in nature [35]. This is consistent with what was observed in the XRD results.

3.6 Transmission electron microscopy (TEM)

The TEM images and size distribution of the ZnO NPs are displayed in Fig. 6. For ZnO-RG1, we can observe agglomerated nanoparticles with size of 43.3 nm and a spherical morphology. Similarly, the images for ZnO-RG2 and ZnO-RG3 also show agglomerated nanoparticles with average sizes of 39.6 nm and 28.0 nm, respectively. We can observe that amount of extract used for the synthesis of the ZnO NPs had a direct influence in their morphology. The samples with a higher concentration of extract show more homogeneous NPs with a narrower size distribution. Notably, in the sample with the highest concentration (ZnO-RG3), the size decreased to 28 nm. This decrease in particle size is due to the biomolecules from *Rubus glaucus* limiting further growth during the NPs formation [41].

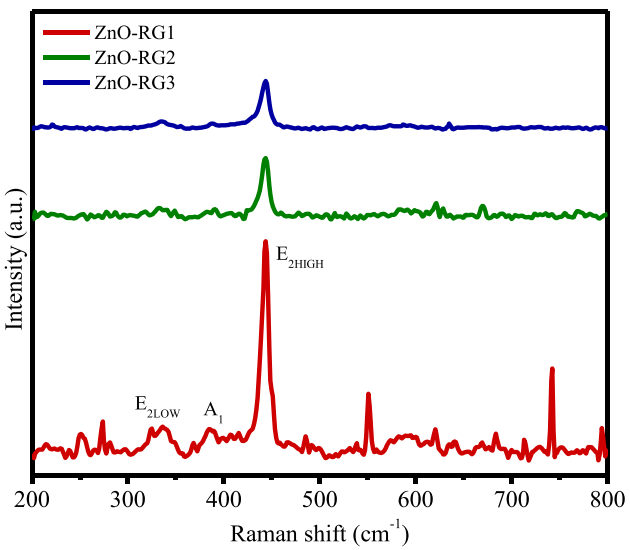

Fig. 5 Raman spectra of the obtained ZnO NPs

3.7 X-ray photoelectron spectroscopy (XPS)

The ZnO NPs were analyzed through XPS to identify the main elements. Wide scans for ZnO-RG1, ZnO-RG2, and ZnO-RG3 are shown in Fig. 7a. For all 3 samples, the main peaks of Zn (Zn2p) and O (O1s) were observed, confirming the synthesis of ZnO [42]. The C1s peak was also observed in all samples, due to residual carbon from the *Rubus glaucus* extract used during synthesis. This is in agreement with the FTIR spectra, which show the presence of several functional groups containing carbon. Meanwhile, the high resolution analysis of the O1s and Zn2p main peaks can be observed in Fig. 7b and c, respectively. The O1s peak for ZnO-RG1 was located at 529.4 eV, and no significant variation was observed in ZnO-RG2 and ZnO-RG3. The Zn2p peak was found with its characteristic doublet ($Zn2p_{1/2}$ and $Zn2p_{3/2}$) at 1043 eV and 1020 eV, respectively. The 23 eV separation between the peaks is characteristic of Zn^{2+} species present in ZnO, and is comparable to previous reports in literature [43].

3.8 Photocatalytic degradation

The results of the solar and UV photocatalytic assay using MB for ZnO-RG1, ZnO-RG2, and ZnO-RG3 are shown in Fig. 8. Once ZnO was irradiated with UV light, we observed 97.4%, 98.5% and 99.9% degradation of MB after 90 min for ZnO-RG1, ZnO-RG2, and ZnO-RG3, respectively. Meanwhile, for samples irradiated with sunlight, we observed 92%, 96%, and 98% degradation of MB after 90 min for ZnO-RG1, ZnO-RG2, and ZnO-RG3, respectively. All three samples showed excellent photocatalytic performance, which can be attributed to oxygen vacancies preventing the recombination of the electron–hole pair [34]. Additionally, we observed an increase in the percentage of photocatalytic degradation for the ZnO NPs prepared using higher extract concentrations. The improved photocatalytic activity confirms that the amount of extract used during the synthesis significantly affects the photocatalytic performance of the ZnO NPs [44].

The results of the solar and UV photocatalytic assay using MO for ZnO-RG1, ZnO-RG2, and ZnO-RG3 are shown in Fig. 9. For the UV light experiment, the ZnO NPs showed degradation of 70%, 90%, and 95% for samples ZnO-RG1, ZnO-RG2, and ZnO-RG3, respectively, after 120 min of exposure to UV light. Meanwhile, for the samples irradiated with sunlight, we observed a degradation of 45%, 70%, and 85% for samples ZnO-RG1, ZnO-RG2, and ZnO-RG3, respectively, for 120 min. ZnO-RG3

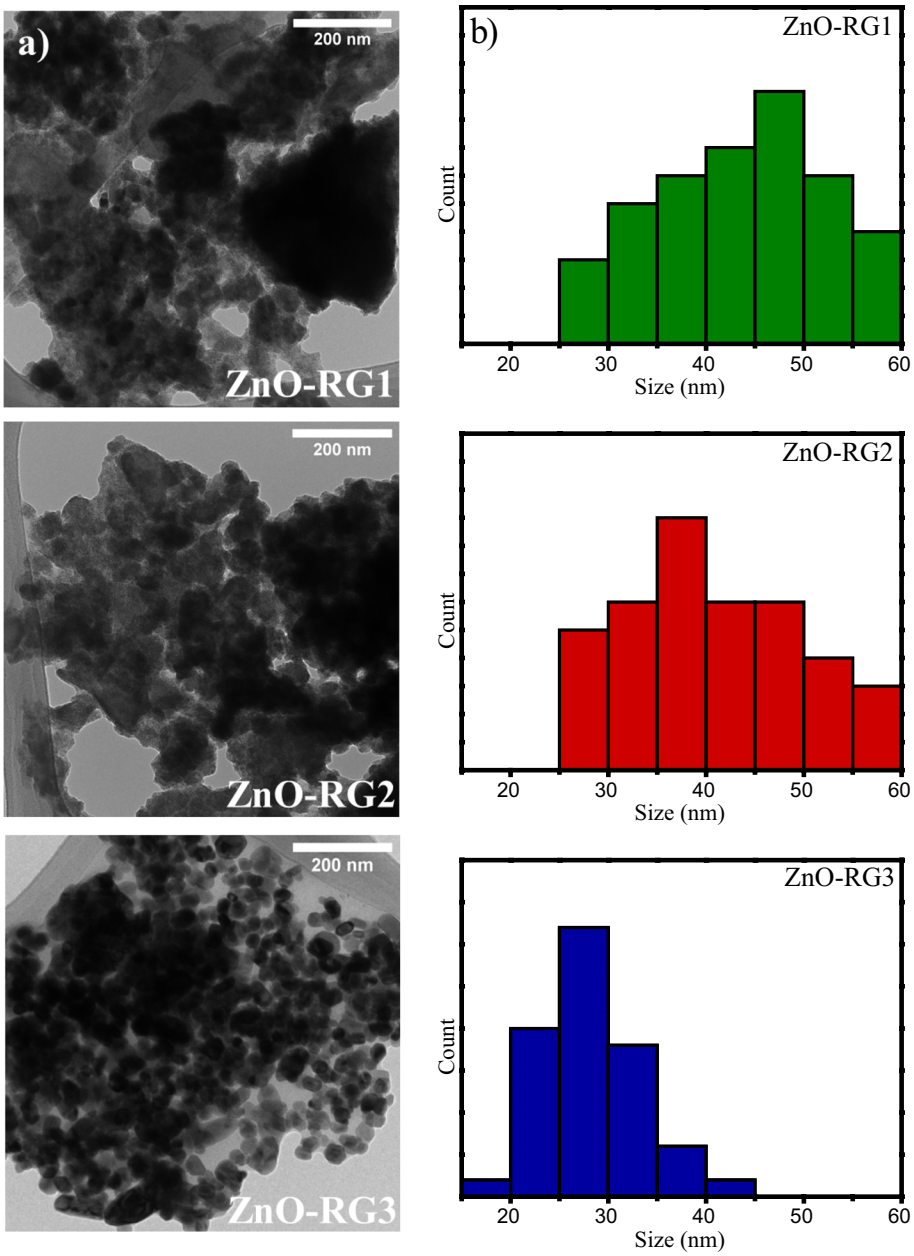

Fig. 6 **a** TEM surface morphology and **b** size distribution of the obtained ZnO NPs

showed the best photocatalytic degradation in both cases, similar to what was observed for MB.

The results of the solar and UV photocatalytic assay using RhB for ZnO-RG1, ZnO-RG2, and ZnO-RG3 are shown in Fig. 10. When irradiated with UV light ZnO-RG1, ZnO-RG2, and ZnO-RG3 presented a degradation of 90%, 93%, and 95% after 120 min, respectively. On the other hand, for the samples irradiated with sunlight, we observed 65%, 85%, and 95% of degradation for ZnO-RG1, ZnO-RG2, and ZnO-RG3 after 120 min. ZnO-RG3 showed excellent photocatalytic degradation, reaching more than 90% degradation of RhB after 120 min of exposure to sunlight.

If we compare the results for the three dyes, we can observe that the ZnO NPs had the lowest efficiency in the degradation of MO. This decreased performance can be attributed to low initial adsorption due to the negative charges of the anionic MO dye, which would be repelled by the negative charge of the residual OH-rich extract molecules in the ZnO NPs, decreasing the photocatalytic efficiency in comparison with the results shown for the MB and RhB dyes, both of which are cationic and thus have more affinity with the organic molecules [44].

The degradation kinetics were analyzed, and the obtained rate constants (k, min^{-1}) for all experiments are summarized in Table 1. All constants were calculated using a first-order

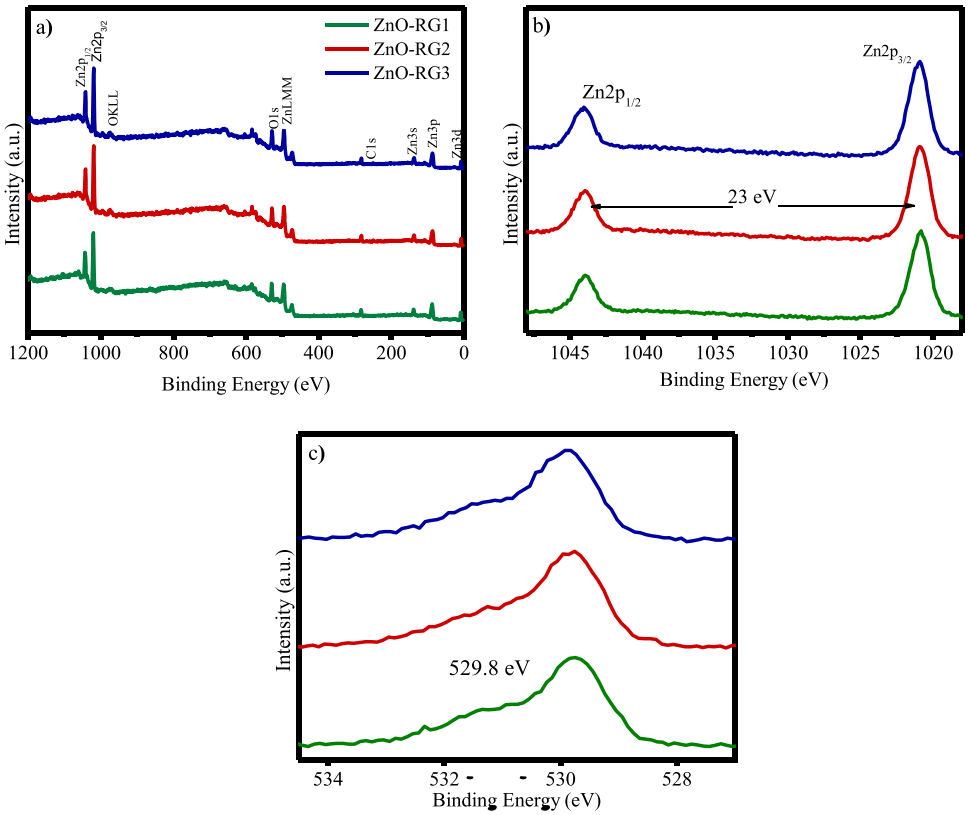

Fig. 7 **a** XPS spectra, and high-resolution analysis of **b** Zn2p and **c** O1s peaks of the obtained ZnO NPs

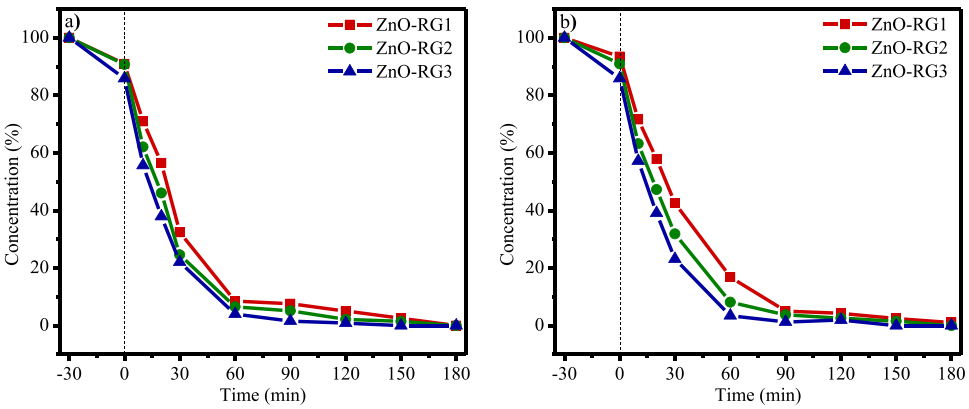

Fig. 8 Photocatalytic degradation of methylene blue under **a** UV and **b** solar irradiation for the obtained ZnO NPs

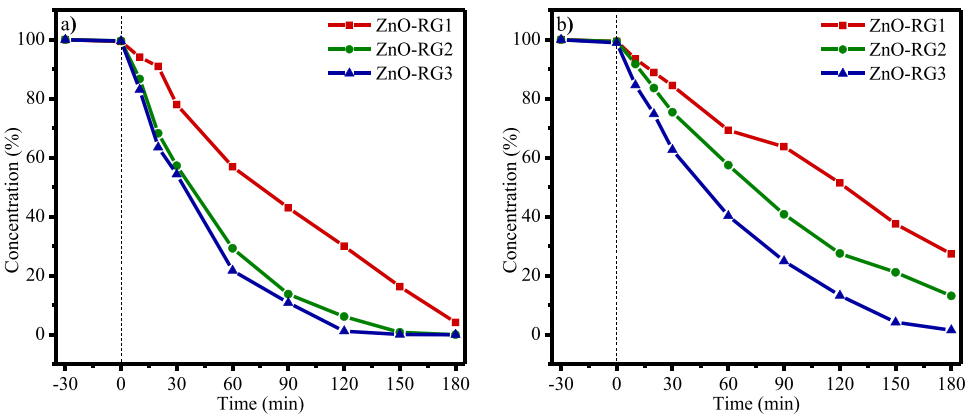

Fig. 9 Photocatalytic degradation of methyl orange under **a** UV and **b** solar irradiation for the obtained ZnO NPs

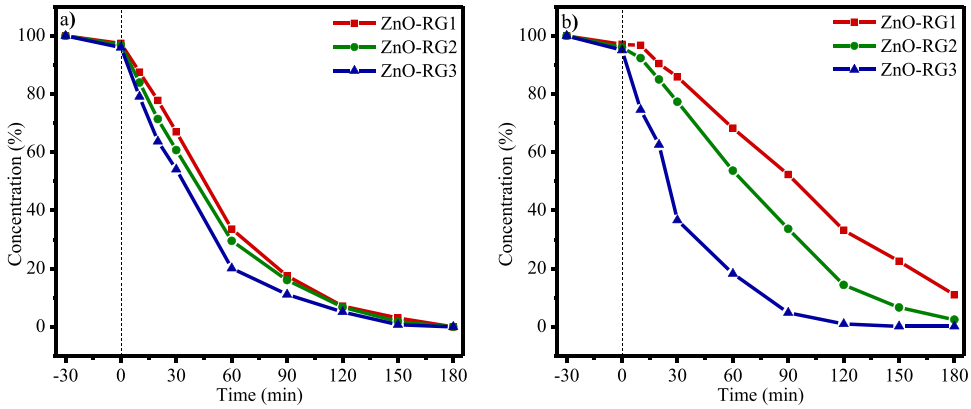

Fig. 10 Photocatalytic degradation of Rhodamine B under **a** UV and **b** solar irradiation for the obtained ZnO NPs

Table 1 Rate constants for the solar and UV photocatalytic degradation of MB, MO, and RhB dyes using the obtained ZnO NPs

Light source	Dye	k (min^{-1})		
		ZnO-RG1	ZnO-RG2	ZnO-RG3
UV	MB	0.01303	0.01983	0.0252
	MO	0.00948	0.0303	0.03241
	RhB	0.01687	0.03221	0.04498
Sunlight	MB	0.01213	0.02245	0.02422
	MO	0.0015	0.00577	0.01641
	RhB	0.00245	0.01015	0.0201

model. According to these values, ZnO-RG3 shows the best photocatalytic performance for all three dyes under both solar and UV irradiation. Compared to the other samples, we can observe that the *k* value was 2.2 times higher for ZnO-RG3 than ZnO-RG1 when degrading MB under solar irradiation, meaning it is twice as efficient. The elevated photocatalytic activity can be mainly attributed to two factors. First, the smaller size of the NPs implies an increase in surface area, which, combined with the presence of oxygen vacancies, increases the active sites available to carry out oxidation reactions. Second, oxygen vacancies generate intermediate energy states which act as charge separators to prevent electron–hole pair recombination, thus improving the efficiency of the material [45, 46].

The proposed mechanism for the degradation of organic dyes using the ZnO NPs is presented in Fig. 11. The process starts when the ZnO NP is irradiated with light of equal or higher energy as the band gap (E_g) value, an electron–hole pair is formed. That is, the electrons (e^-) in the valence band (VB) become excited and are transferred to the conduction band (BC) of the photocatalyst, leaving a hole (h^+) in the BV (Eq. 1). The e^- in the CB then interact with the O_2 molecules present to generate reactive oxygen radicals (Eqs. 2 and 3). Meanwhile, holes in the valence band interact with H_2O molecules to generate OH radicals (Eq. 4). Then these highly reactive species interact with the organic dyes, breaking them down into successively smaller compounds, until they finally degrade into CO_2, H_2O and other mineralized by-products (Eqs. 5 and 6) [47].

$$\mathrm{ZnO} + h\nu\left(\mathrm{Energy} \geq E_g\right) \rightarrow \mathrm{ZnO}\left(e^-_{\mathrm{CBZnO}}\right) + \mathrm{ZnO}\left(h^+_{\mathrm{VBZnO}}\right) \quad (1)$$

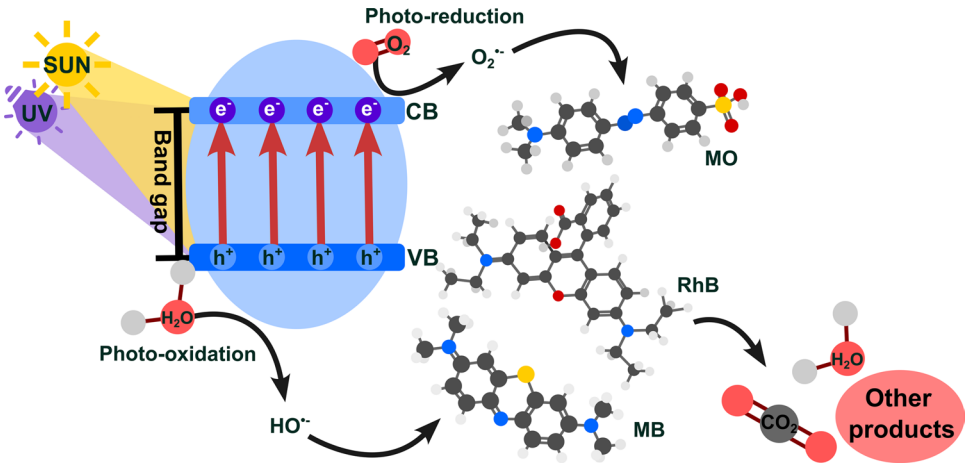

Fig. 11 Schematic of the proposed mechanism for photocatalytic degradation of organic dyes using the ZnO NPs

Table 2 Green synthesis of ZnO NPs and their efficiency in the photodegradation of synthetic dyes

Light source	Extract	Dye	Degradation (%)	Degradation time (min)	Year	References
UV	*Rubus glaucus*	MB	96	60	2023	This work
	Rubus glaucus	MO	98	90	2023	This work
	Rubus glaucus	RhB	93	90	2023	This work
	Salvia officinalis	MO	92	120	2021	[48]
	Salvadora persica	MB	95	150	2020	[37]
	Pithecellobium dulce	MB	63	120	2018	[49]
	Carica papaya	MB	100	180	2017	[50]
SOLAR	*Rubus glaucus*	MB	97	60	2023	This work
	Rubus glaucus	MO	96	150	2023	This work
	Rubus glaucus	RhB	96	90	2023	This work
	Alchemilla vulgaris	RhB	75	120	2021	[51]
	Canna indica L	MB	90	150	2021	[44]
	Cannabis sativa	MO	35	80	2020	[52]
	Cyanometra ramiflora	RhB	98	200	2019	[53]
	Scutellaria baicalensis	MB	98	210	2019	[54]

$$\mathrm{ZnO}\left(e^{-}_{\mathrm{CBZnO}}\right) + \mathrm{O_2} \rightarrow \mathrm{ZnO/Dye} + \mathrm{O_2^{\cdot}} \quad (2)$$

$$\mathrm{O_2^{\cdot}} + \mathrm{H_2O} \rightarrow \mathrm{OH^{\cdot}} \quad (3)$$

$$\mathrm{ZnO}\left(h^{+}_{\mathrm{VBZnO}}\right) + \mathrm{H_2O} \rightarrow \mathrm{ZnO} + \mathrm{OH^{\cdot}} \quad (4)$$

$$\mathrm{OH^{\cdot}} + \mathrm{Dye} \rightarrow \mathrm{H_2O} + \mathrm{CO_2} + \mathrm{Other\ subproducts} \quad (5)$$

$$\mathrm{O_2^{\cdot}} + \mathrm{Dye} \rightarrow \mathrm{H_2O} + \mathrm{CO_2} + \mathrm{Other\ subproducts} \quad (6)$$

Table 2 shows the photocatalytic performance of the three dyes compared with those reported in other studies.

4 Conclusions

In this study, we successfully synthesized ZnO NPs using *Rubus glaucus* extract as a chelating agent. The characterization results revealed the presence of wurtzite phase spherical ZnO NPs, and notably, they confirmed that the *Rubus glaucus* extract directly influenced the optical properties of the ZnO NPs due to the introduction of oxygen vacancies, which resulted in a decrease in the band gap (from 2.88 to 2.54 eV) as the amount of extract used for synthesis increased. Furthermore, the photocatalytic assay showed that the obtained ZnO NPs have good photocatalytic activity under sunlight and UV light. We found that ZnO-RG3 had the best performance. It removed 90% of MB after 60 min of sunlight exposure, 90% of MO in 90 min, and 90% of RhB in 120 min. The results obtained in this study demonstrate that using *Rubus glaucus* extract as a chelating agent provides a simple, sustainable, and cost-efficient procedure to obtain visible-light photocatalysts able to degrade various pollutants and other potential applications.

Acknowledgements The authors thank the projects of the Autonomous University of Baja California (UABC) 402/3391 and 402/3751, as well as 402/1/C/58/24. This research was funded by the Frontera Science Project with number CF-2023-I-1805 of CONAHCyT. Thanks to the Convocatoria Movilidad Académica 2023-UABC. The authors acknowledge to Dr. Uvaldo Hernández and B.Sc. María Citlalit Martínez Soto for technical assistance during this work.

Author contributions E. Silva: Investigation, Methodology, and Writing—Original Draft. V.M. Orozco-Carmona: Conceptualization, Formal Analysis and Writing—Review & Editing. A. Castro-Beltran: Visualization, Investigation, and Writing—Review & Editing. P.A. Luque: Formal analysis, Supervision, Validation, and Writing—Review & Editing.

Data availability All data generated or analysed during this study are included in this published article.

Declarations

Conflict of interest The authors have no competing interests to declare that are relevant to the content of this article.

References

1. L.C. Stringer, A. Mirzabaev, T.A. Benjaminsen, R.M.B. Harris, M. Jafari, T.K. Lissner, N. Stevens, C. Tirado-von der Pahlen, One Earth **4**, 851 (2021)
2. A. Hogan, M. Young, Camb. J. Reg. Econ. Soc. **6**, 319 (2013)
3. H. Qadri, R. Ahmad, B. Mohammad, A. Mehmood, G. Hamid, *Fresh water pollution dynamics and remediation* (Springer Singapore, Singapore, 2020)

4. N.M. Sivaram, P.M. Gopal, D. Barik, *Energy from toxic organic waste for heat and power generation* (Elsevier, 2019), pp.43–54
5. A.G. Acedo-Mendoza, A. Infantes-Molina, D. Vargas-Hernández, C.A. Chávez-Sánchez, E. Rodríguez-Castellón, J.C. Tánori-Córdova, Mater. Sci. Semicond. Process. **119**, 105257 (2020)
6. L. Bilińska, M. Gmurek, S. Ledakowicz, Chem. Eng. J. **306**, 550 (2016)
7. M. Arif, M.Z.U. Shah, S.A. Ahmad, M.S. Shah, Z. Ali, A. Ullah, M. Idrees, J. Zeb, P. Song, T. Huang, J. Yi, Opt Mater (Amst) **134**, 113135 (2022)
8. C.H. Nguyen, C.C. Fu, R.S. Juang, J. Clean. Prod. **202**, 413 (2018)
9. P.C. Nagajyothi, S.V. Prabhakar-Vattikuti, K.C. Devarayapalli, K. Yoo, J. Shim, T.V.M. Sreekanth, Crit. Rev. Environ. Sci. Technol. **50**, 2617 (2020)
10. J. Ebrahimian, M. Mohsennia, M. Khayatkashani, Opt. Mater. (Amst.) **120**, 111404 (2021)
11. G.K. Weldegebrieal, Inorg. Chem. Commun. **120**, 108140 (2020)
12. M. Ahmad, M.T. Qureshi, W. Rehman, N.H. Alotaibi, A. Gul, R.S. Abdel-Hameed, M. Al-Elaimi, M.F.H. Abd-El-Kader, M. Nawaz, R. Ullah, J. Alloys Compd. **895**, 162636 (2022)
13. T. Bi, Z. Du, S. Chen, H. He, X. Shen, Y. Fu, Appl. Surf. Sci. **614**, 156240 (2023)
14. N. Belachew, M.H. Kahsay, A. Tadesse, K. Basavaiah, J. Environ. Chem. Eng. **8**, 104106 (2020)
15. N. Ullah, M.T. Qureshi, A.M. Toufiq, F. Ullah, M. Al-Elaimi, R.S.A. Hameed, A. Khan, H.M.E. Ragab, Appl. Phys. A Mater. Sci. Process. **127**, 1 (2021)
16. Y. Zhao, L. Liu, T. Cui, G. Tong, W. Wu, Appl. Surf. Sci. **412**, 58 (2017)
17. M. Kashif, Z. Ngaini, A.V. Harry, R.L. Vekariya, A. Ahmad, Z. Zuo, S.K. Sahari, S. Hussain, Z.A. Khan, A. Alarifi, Appl. Phys. A Mater. Sci. Process. **126**, 1 (2020)
18. G. Sharmila, M. Thirumarimurugan, C. Muthukumaran, Microchem. J. **145**, 578 (2019)
19. G.A. Naikoo, M. Mustaqeem, I.U. Hassan, T. Awan, F. Arshad, H. Salim, A. Qurashi, J. Saudi Chem. Soc. **25**, 101304 (2021)
20. M.S. Othman, S.T. Obeidat, G.M. Aleid, A.H. Al-Bagawi, M.A. Fareid, R.A. Hameed, K.M. Mohamed, M.S. Abdelfattah, A. Fehaid, M.M. Hussein, S.M.H. Aboelnaga, A.E. Abdel-Moneim, Appl. Sci. (Switzerland) **13**, 1050 (2023)
21. T. Iqbal, K. Munir, S. Afsheen, M. Zafar, M. Abrar, M.T. Qureshi, M. Al-Elaimi, R.A. Hameed, R. Chand, G. Yunus, J. Inorg. Organomet. Polym. Mater. **32**, 2221 (2022)
22. R. Abdel Hameed, M. Faride, M. Othman, B. Huwaimel, S. Al-Mhyawi, A. Shamroukh, F. Alshammary, E. Aljuhani, M. Abdallah, http://www.mc.manuscriptcentral.com/Tgcl **15**, 847 (2022)
23. V.C. Téllez, M.C. Portillo, H.J. Santiesteban, M.P. Castillo, A.C. Santiago, M.A. Mora-Ramírez, H.A. Coyotecatl, O.P. Moreno, Opt. Mater. (Amst.) **112**, 110747 (2021)
24. M. Ospina, K. Montaña-Oviedo, Á. Díaz-Duque, H. Toloza-Daza, C.-E. Narváez-Cuenca, Food Chem. **281**, 114 (2019)
25. P.C. Nagajyothi, P. Muthuraman, T.V.M. Sreekanth, D.H. Kim, J. Shim, Arab. J. Chem. **10**, 215 (2017)
26. I. Samaniego, B. Brito, W. Viera, A. Cabrera, W. Llerena, T. Kannangara, R. Vilcacundo, I. Angós, W. Carrillo, Plants **9**, 1027 (2020)
27. B. Kumar, K. Smita, L. Cumbal, A. Debut, Y. Angulo, J. Saudi Chem. Soc. **21**, S475 (2017)
28. M. Ahmad, W. Rehman, M.M. Khan, M.T. Qureshi, A. Gul, S. Haq, R. Ullah, A. Rab, F. Menaa, J. Environ. Chem. Eng. **9**, 104725 (2021)
29. F. Davar, A. Majedi, A. Mirzaei, J. Am. Ceram. Soc. **98**, 1739 (2015)
30. A. Diallo, B.D. Ngom, E. Park, M. Maaza, J. Alloys Compd. **646**, 425 (2015)
31. S. Baset, H. Akbari, H. Zeynali, M. Shafie, Dig. J. Nanomater. Biostruct. **6**, 709 (2011)
32. A. Dolgonos, T.O. Mason, K.R. Poeppelmeier, J. Solid State Chem. **240**, 43 (2016)
33. B. Babu, I. Neelakanta-Reddy, K. Yoo, D. Kim, J. Shim, Mater. Lett. **221**, 211 (2018)
34. H. Li, J. Liu, C. Wang, H. Yang, X. Xue, Vacuum **199**, 110891 (2022)
35. M.I. Benitez-Salazar, V.E. Niño-Castaño, R.A. Dueñas-Cuellar, L. Caldas-Arias, I. Fernández, J.E. Rodríguez-Páez, J. Environ. Chem. Eng. **9**, 106544 (2021)
36. F. Jones, H. Tran, D. Lindberg, L. Zhao, M. Hupa, Energy Fuels **27**, 5663 (2013)
37. F.A. Alharthi, A.A. Alghamdi, A.A. Alothman, Z.M. Almarhoon, M.F. Alsulaiman, N. Al-Zaqri, Crystals (Basel) **10**, 441 (2020)
38. X. Wang, H. Xu, Y. Zhang, X. Ji, R. Zhang, Ceram. Int. **47**, 16170 (2021)
39. C. Tiwari, A. Pandey, A. Dixit, Thin Solid Films **762**, 139539 (2022)
40. A.F. Jaramillo, R. Baez-Cruz, L.F. Montoya, C. Medina, E. Pérez-Tijerina, F. Salazar, D. Rojas, M.F. Melendrez, Ceram. Int. **43**, 11838 (2017)
41. N. Matinise, X.G. Fuku, K. Kaviyarasu, N. Mayedwa, M. Maaza, Appl. Surf. Sci. **406**, 339 (2017)
42. A.G. Marrani, F. Caprioli, A. Boccia, R. Zanoni, F. Decker, J. Solid State Electrochem. **18**, 505 (2014)
43. H.-Y. Lee, B.-K. Wu, M.-Y. Chern, Electron. Mater. Lett. **10**, 51 (2014)
44. D.T.C. Nguyen, H.T.N. Le, T.T. Nguyen, T.T.T. Nguyen, L.G. Bach, T.D. Nguyen, T. van Tran, J. Hazard. Mater. **420**, 126586 (2021)
45. K. Gowthaman, P. Gowthaman, M. Venkatachalam, M. Saroja, M. Kutraleeswaran, S. Dhinesh, Inorg. Chem. Commun. **146**, 110197 (2022)
46. Y. Tang, H. Zhou, K. Zhang, J. Ding, T. Fan, D. Zhang, Chem. Eng. J. **262**, 260 (2015)
47. J. Liu, Y. Wang, J. Ma, Y. Peng, A. Wang, J. Alloys Compd. **783**, 898 (2019)
48. M.A. Abomuti, E.Y. Danish, A. Firoz, N. Hasan, M.A. Malik, Biology **10**, 1075 (2021)
49. G. Madhumitha, J. Fowsiya, N. Gupta, A. Kumar, M. Singh, J. Phys. Chem. Solids **127**, 43 (2019)
50. R. Rathnasamy, P. Thangasamy, R. Thangamuthu, S. Sampath, V. Alagan, J. Mater. Sci. Mater. Electron. **28**, 10374 (2017)
51. S. Rajendrachari, P. Taslimi, A.C. Karaoglanli, O. Uzun, E. Alp, G.K. Jayaprakash, Arab. J. Chem. **14**, 103180 (2021)
52. A. Chauhan, R. Verma, S. Kumari, A. Sharma, P. Shandilya, X. Li, K.M. Batoo, A. Imran, S. Kulshrestha, R. Kumar, Sci. Reports **10**, 1 (2020)
53. T. Varadavenkatesan, E. Lyubchik, S. Pai, A. Pugazhendhi, R. Vinayagam, R. Selvaraj, J. Photochem. Photobiol. B. **199**, 111621 (2019)
54. L. Chen, I. Batjikh, J. Hurh, Y. Han, Y. Huo, H. Ali, J.F. Li, E.J. Rupa, J.C. Ahn, R. Mathiyalagan, D.C. Yang, Optik (Stuttg) **184**, 324 (2019)